

Cite this: *J. Mater. Chem. A*, 2019, 7, 3375

Enhanced cycling stability of boron-doped lithium-rich layered oxide cathode materials by suppressing transition metal migration†

Zhenhe Sun,^a Lingqun Xu,^a Caiqiao Dong,^a Hongtao Zhang,^{ab} Mingtao Zhang,^{id a} Yiyang Liu,^a Ying Zhou,^a Yu Han^a and Yongsheng Chen^{id *ab}

Lithium-rich layered oxide (LLO) has been considered as an attractive candidate due to its high capacitive performance. However, its practical applications are hindered by voltage/capacity fading, low initial coulombic efficiency, and non-negligible Mn²⁺ dissolution. Herein, we have prepared boron-doped LLO (LLO@LBO) with excellent cycle/voltage retention and improved initial coulombic efficiency by a facile synthesis process. First-principles calculations and *ex situ* XRD have clarified that the incorporation of boron atoms in the tetrahedral interstices can effectively impede the migration channel of the transition metal ions. The strong B–O bonds can enhance the structural stability of LLO@LBO. Furthermore, the boron doping technique can suppress Mn²⁺ dissolution in LLO@LBO during cycling and improve the life time of the cathode and anode electrodes simultaneously. In the lithium ion battery cathode tests, the LLO@LBO delivers a reversible capacity of 293.9 mA h g⁻¹ with a capacity retention of 89.5% at 0.5C after 100 cycles. The full cell test shows an initial energy density of 472.1 W h kg⁻¹ with excellent energy retention of 84.1% after 150 cycles.

Received 8th November 2018
Accepted 9th January 2019

DOI: 10.1039/c8ta10786f

rsc.li/materials-a

Introduction

Lithium-ion batteries (LIBs) have proved to be one of the most promising energy storage devices to power electric vehicles (EVs), and hybrid electric vehicles (HEVs) due to their high energy density and long cycle life.¹ Nevertheless, the dissatisfactory energy density of LIBs still limits their driving range and practical application.² It is generally believed that the capacity of the cathode materials is one of the major factors that contribute to the performance of LIBs.^{3,4} With regard to this viewpoint, LLO materials such as Li_{1+x}TM_{1-x}O₂ (TM = transition metal, Mn, Ni or Co) have become a possible future choice because of their high specific capacity and low cost.^{5–7} However, LLOs suffer from fundamental problems including serious voltage/capacity fading, low initial coulombic efficiency and non-negligible Mn²⁺ dissolution to some extent.^{8,9} Great efforts have been made to settle these problems.^{10–14}

Doping with foreign ions is a common strategy to suppress phase transformation and mitigate voltage fading. For example, monovalent metal ions,^{11,15} multivalent cations,^{16,17} F⁻ anions,¹⁸ polyanions,¹⁹ *etc.* can be incorporated into the lattice sites of the

cathode materials. Monovalent metal ions usually have larger atomic radii, thus only small amounts of Na⁺ and K⁺ are sufficient to increase the slab space of Li⁺ and also accelerate Li⁺ transport during cycling.^{10,11} Multivalent cations, such as Al³⁺ and Ti⁴⁺, can be doped by replacing the intrinsic transition metal ions.^{16,20} Moreover, foreign multivalent cations can block the TM migration path owing to their larger atomic radii or enhance the structural stability by forming stronger bonds with oxygen.¹⁷ Simple doping with F⁻ anions has also been extensively studied and it can suppress the formation of oxygen vacancies in the first charging process.^{21,22} Besides, F⁻ cannot provide equal negative charges compared to O²⁻, which may induce the partial reduction of TMs and provide extra capacity.^{18,23} Polyanion doping, including PO₄³⁻,¹⁹ SO₄²⁻, SiO₄⁴⁻,²⁴ and BO₃³⁻,²⁵ can lower the energy of the O 2p band compared to the pristine layered oxides and limit the evolution of oxygen.²⁶ The strong covalent bonding of X–O (X = P, S, Si, and B) can improve the thermal and structural stability obviously. However, incorporation of such inactive atoms usually results in lowered specific capacity.²⁷

Among them, boron atoms have the lightest atomic mass which can reduce the adverse impact resulting from the incorporation of inactive atoms to some extent. As we know, TM ions can migrate from the octahedral sites of the TM layers to the tetrahedral sites of the Li layer then further migrate to the octahedral sites of the Li layer.¹⁰ Due to the small radius of boron (0.27 Å), it can be intercalated into the tetrahedral sites of the TM layer.²⁸ Recently, it has been demonstrated that the

^aThe Centre of Nanoscale Science and Technology, Key Laboratory of Functional Polymer Materials, Nankai University, Tianjin, 300071, China

^bThe National Institute for Advanced Materials, Nankai University, Tianjin 300071, China. E-mail: yschen99@nankai.edu.cn

† Electronic supplementary information (ESI) available. See DOI: 10.1039/c8ta10786f

introduction of boron atoms can impede the path and then prevent the phase transformation from a layered structure to a spinel structure.^{25,28,29} However, the electrochemical performance enhancing mechanism of boron doping is still elusive. In addition, the doping methods previously used, such as the sol-gel process, require rather complex synthetic routes which limit their practical application.^{30–32} Besides, the full cell performance is needed to evaluate reliably the material performance, which is still missing.

Herein, we present boron-doped LLOs *via* a facile preparation method using LiBO₂ as the boron source. The structural and electrochemical performances of LLOs with and without boron doping were compared comprehensively. The electrochemical performance enhancing mechanism of boron is systematically investigated and understood using both experimental and theoretical approaches, including the first-principles calculation and *ex situ* XRD (X-ray diffraction). These results above indicate that strong B–O bonds can enhance the structural stability of LLO@LBO, and suppress Mn migration and dissolution in LLO@LBO for the life time. With these, the doped material LLO@LBO delivers a reversible capacity of 293.9 mA h g⁻¹ with a capacity retention of 89.5% at 0.5C after 100 cycles. Furthermore, when combined with an anode material SnO₂, the full battery cell shows a high initial energy density (472.1 W h kg⁻¹) with excellent energy retention (84.1% retention after 150 cycles at 0.5C).

Results and discussion

Structure and morphology characterization

We obtained the boron doped LLO by a facile solid reaction at high temperature using LiBO₂ as the boron source. The detailed preparation process is shown in the Experimental section. Fig. 1 shows the XRD patterns of Li_{1.2}Ni_{0.13}Co_{0.13}Mn_{0.54}B_xO₂ ($x = 0, 0.005, 0.0125$ and 0.02). All peaks are indexed on the basis of the α -NaFeO₂ structure with the space group $R\bar{3}m$ of layered LiTMO₂

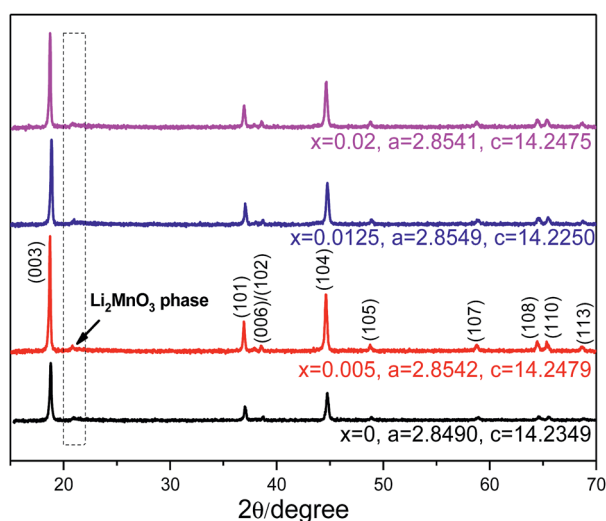


Fig. 1 XRD patterns of Li_{1.2}Ni_{0.13}Co_{0.13}Mn_{0.54}B_xO₂ ($x = 0, 0.005, 0.0125$ and 0.02).

(TM = Ni, Co, and Mn).³³ The weak, broad peaks at 21–23° are attributed to the LiMn₆ superstructure of the monoclinic Li₂MnO₃ phase with $C2/m$ symmetry. A high (003)/(104) peak intensity ratio (>1.2) was observed clearly, suggesting a low degree of TM ions in the Li layers.³⁴ The clear peak separation between (006)/(102) and (108)/(110) demonstrates a well-crystallized layered structure.³⁵ In the XRD patterns of the boron-doped compound, no extra peak compared to that without B doping indicates that the boron atoms are incorporated into the lattice of Li_{1.2}Ni_{0.13}Co_{0.13}Mn_{0.54}B_xO₂. Furthermore, doping LLOs with boron does not change its intrinsic layered structure. The unit cell parameters (a and c) of bare LLOs and B-doped LLOs have no visible difference. Besides, the XRD results have been refined to further study the effect of boron doping on the lattice structure (Table S1 and Fig. S1, ESI†). By comparison of the refinement results of LLO with and without boron doping, it is concluded that the position of oxygen atoms changes slightly, which is influenced by the doped boron atoms. Besides, the Li/Ni mixing increases slightly after boron doping, which is possibly induced by the high treatment temperature (700 °C) in the doping process. The atomic occupancies for 3a and 6c sites are unchanged. These results can be explained as the boron atoms are located in crystallographic sites instead of the constituent atoms in LLOs.³⁶

To explore the effect of boron doping on the morphology and structure of Li_{1.2}Ni_{0.13}Co_{0.13}Mn_{0.54}B_xO₂ (LLO@LBO, taking $x = 0.0125$ as an example), the as-prepared samples were characterized by SEM (scanning electron microscopy), TEM (transmission electron microscopy) and XPS (X-ray photoelectron spectroscopy). The spherical LLO@LBO cathode particles show a radius range of 3–5 μm and are different from the brick-like morphology of LLO (Fig. S2, ESI†). Moreover, the primary particles turn out to be irregular after boron doping (Fig. S2, ESI†). This results from the ball-milling and calcination during the preparation process. The TEM images of LLO and LLO@LBO (individual particles) have been shown in Fig. S3.† There are some impurities at the surface of LLO@LBO attributed to the residual oxidation product LiBO₂. Fig. 2a shows the surface structure of LLO@LBO from TEM. We can easily find two different sets of lattice fringes, corresponding to (003) planes of the $R\bar{3}m$ structure and (200) planes of the $C2/m$ structure both related to layered LLO@LBO. These are consistent with the XRD results (Fig. 1). The TEM-EDS (Energy Dispersive Spectrum) mapping (Fig. 2b–f) demonstrates that the distribution of Mn, Ni, Co, and O is uniform, indicating that the introduction of boron atoms has little effect on the distribution of TMs. The elemental composition of the surface and bulk LLO@LBO is further analysed by Ar⁺ etching. Fig. 2g shows the B 1s spectra of LLO@LBO at different etching depths (0, 25, 50, 75, and 100 nm). A sharp peak at around 191 eV was observed which corresponds to the presence of boron atoms.³⁶ However, we observed that the B 1s spectra at the surface (0 nm) shifted to the high bonding energy region (191.8 eV) compared to those at other depths. It is also found that O 1s spectra (Fig. 2h) show a similar tendency. To explain this in detail, the XPS characterization of B 1s in LiBO₂ and its possible oxidation product (B₂O₃) is supplied in Fig. S4.† It is obvious that the B 1s peak

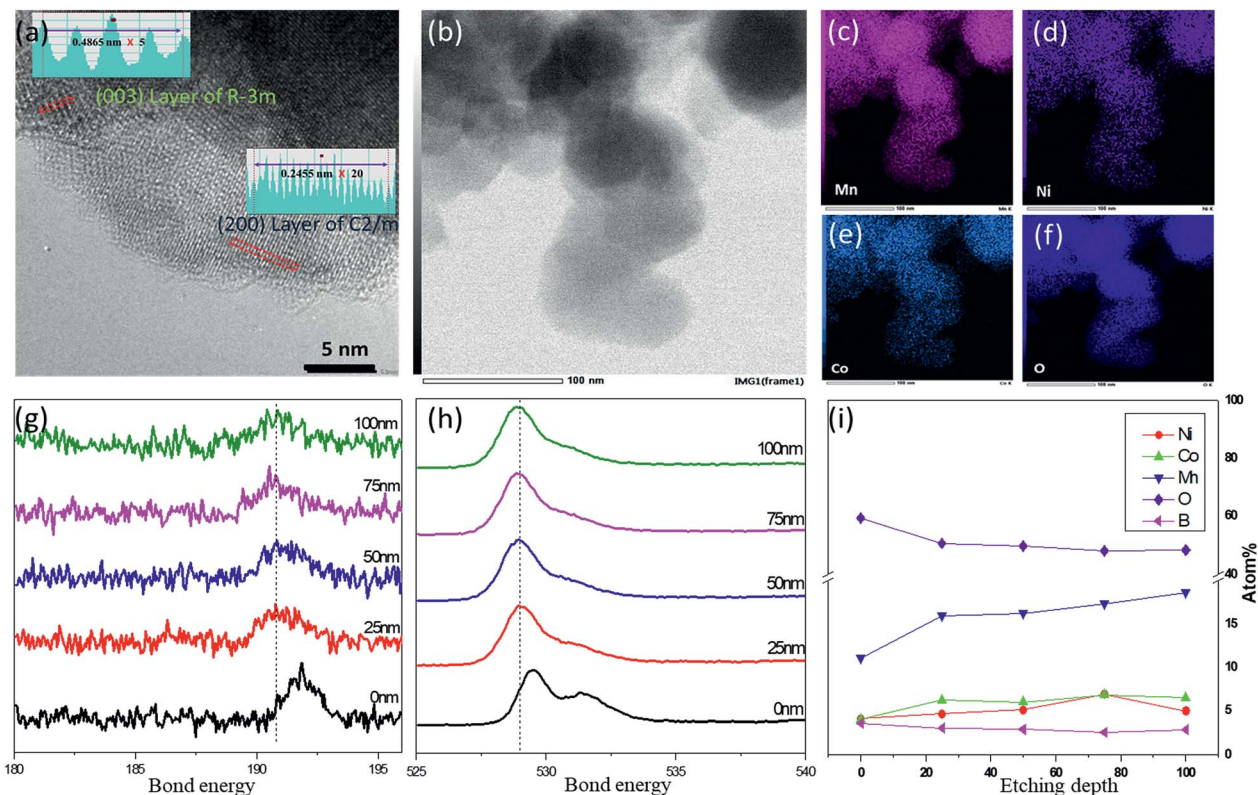


Fig. 2 (a) The HR-TEM pattern of LLO@LBO, (b) the morphology of LLO@LBO and the EDS mapping of (c) Mn, (d) Ni, (e) Co, and (f) O. XPS spectra of (g) B 1s and (h) O 1s at different etching depths (0 nm, 25 nm, 50 nm, 75 nm and 100 nm). (i) Content of Ni, Co, Mn and B at different etching depths.

position (191.8 eV) of LLO@LBO at the surface is different from that of LiBO_2 (194.2 eV). This means different chemical environments for boron atoms in LLO@LBO and LiBO_2 . The B 1s in B_2O_3 is around 192 eV, slightly higher than that in LLO@LBO at the surface. Thus, it is possible that the residual oxidation product LiBO_2 induces B 1s peak shift to a higher bond energy region (Fig. S3 and S4, ESI†). Considering the obvious difference between B 1s in the bulk of LLO@LBO (around 191 eV) and B_2O_3 (192 eV), it is believed that the boron atoms in the bulk of LLO@LBO show different chemical environments compared to those in the latter.³⁷ Importantly, the concentration of boron shows no meaningful change in the bulk structure while that at the surface region shows a slight increase likely due to the residual oxidation product LiBO_2 (Fig. 2i and S3, ESI†). Moreover, the valence states of transition metals (Ni, Co and Mn) remain the same before and after boron doping, supported by XPS results (Fig. S5, ESI†).

FT-IR is conducted as the supplement of the XPS test to further study the variation of the M–O bond after boron doping (Fig. S6, ESI†). The characteristic peaks at 622.97 and 545.82 cm^{-1} are attributed to the O–M–O bending and the M–O asymmetric stretching modes in MO_6 octahedra, respectively. After boron doping, the bending and stretching mode frequencies shift slightly to lower wavenumber regions, indicating that the M–O covalency in LLOs is decreased after boron doping. This is favourable for stabilization of the host lattice in LLOs.³⁸ Otherwise, an extra peak at 867.91 cm^{-1} is found for

LLO@LBO, which is attributed to the asymmetric stretching mode of four-coordinated BO_4 .³⁹

These results indicate that the boron atoms have been successfully doped into LLO with a uniform distribution and the crystal structure and transition metal valence remain unchanged.

Electrochemical results and discussion

A series of materials with different B doping amounts and preparation conditions have been investigated (Fig. S7, ESI†) and the optimized material was obtained in the ratio of $\text{Li}_{1.2}\text{Ni}_{0.13}\text{Co}_{0.13}\text{Mn}_{0.54}\text{B}_x\text{O}_2$ with $x = 0.0125$ prepared at the reaction temperature of 700 °C. Unless otherwise specified, this material, short named as LLO@LBO, was chosen for further studies.

The electrochemical charge/discharge measurements of LLO and LLO@LBO were carried out using Li metal as the counter electrode between 2.0 and 4.6 V at constant current 0.5C ($1\text{C} = 200\text{ mA g}^{-1}$). The initial charge curves of LLO and LLO@LBO are composed of a slope region below 4.5 V, followed by a voltage plateau at around 4.5 V (Fig. 3a). The slope region results from the oxidation of TMs (Co^{3+} and Ni^{2+}) and the voltage plateau is related to the activation of the Li_2MnO_3 phase and oxygen redox, which is close to the extra specific capacity for LLO cathode materials.¹¹ For LLO and LLO@LBO, the specific capacities of the slope region are similar. But the voltage plateau of LLO@LBO is a little shorter than that of LLO. This is

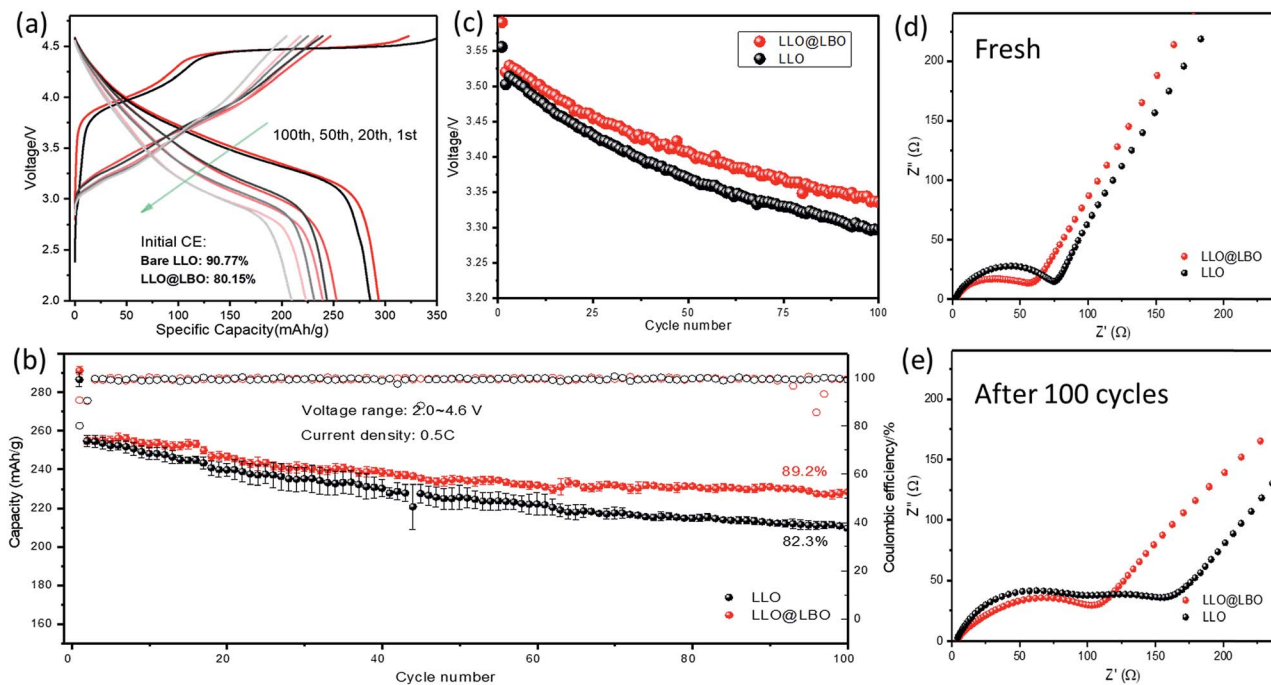


Fig. 3 Electrochemical performance of LLO and LLO@LBO. (a) Charge/discharge profile at the 1st, 20th, 50th and 100th cycle, (b) cycle performance and coulombic efficiency comparison of LLO@LBO and (c) average discharge potential versus cycle number plots. EIS spectra of the LLO electrode and LLO@LBO electrode (d) before cycling and (e) after 100 cycles.

due to suppressed side reactions resulting from the strong B–O bond which stabilizes the oxygen framework of LLO@LBO.²⁹ The mass of introduced boron atoms is only 0.16 wt% of the host, far lower than the LLOs with other multivalent ion doping (Table S2[†]). As a result, LLO@LBO shows a lower initial charge capacity (322.6 mA h g⁻¹) but a higher discharge capacity (293.9 mA h g⁻¹) compared to those of LLO (355.4 and 285.6 mA h g⁻¹, respectively). Initial coulombic efficiency increases from 80.15% to 90.77% after boron doping. The enhanced reversible capacity and initial coulombic efficiency are superior to those of most previous studies (Table S2[†]). Fig. 3b shows the cycling performance of the cells at 0.5C rate. LLO@LBO shows obviously enhanced cycle stability. A much larger discharge capacity of 228.55 mA h g⁻¹ was obtained after 100 cycles, corresponding to a capacity retention of 89.5%. In contrast, the discharge capacity of LLO decreases from 254.72 mA h g⁻¹ to 209.6 mA h g⁻¹ after 100 cycles with a capacity retention of 82.3%. To estimate the voltage fading, the average voltage is calculated based on cycling data at room temperature (Fig. 3c). The average voltage of LLO@LBO decreases from 3.5291 V to 3.3355 V after 100 cycles, 1.936 mV per cycle, significantly decreased from 2.163 mV for the case of LLO. The reasons for suppressed voltage fading will be discussed in the next section.

Electrochemical impedance spectra (EIS) were measured to explore the origin of the improvement in the electrochemical performance of LLO@LBO. Nyquist plots of LLO and LLO@LBO electrodes are compared before charging (Fig. 3d) and after 100 cycles at 0.5C (Fig. 3e). The plots of LLO and LLO@LBO before charging consist of a semicircle in the intermediate-frequency

region and a sloped straight line in the low-frequency region. The semicircle in the intermediate-frequency region is correlated with the charge-transfer (R_{ct}) process, and the straight line in the low-frequency region is related to the solid-state diffusion (Warburg impedance, Z_w) of Li ions in the active materials.^{6,20} When there are two semicircles in the Nyquist plot, as in this case, the semicircle at high frequency belongs to the surface layer resistance (R_{si}) resulting from the solid electrolyte interface (SEI) while the other semicircle at low frequency is related to R_{ct} . The equivalent circuits are shown in Fig. S8[†] and the simulated results are shown in Table S3.[†] Before charging, the R_{ct} value of the LLO electrode is 79.55 Ω while the LLO@LBO electrode exhibits a smaller R_{ct} value of 56.64 Ω . The diffusion coefficient of Li⁺ has been calculated in Fig. S9[†] based on the EIS results. After boron doping, the diffusion coefficient of Li⁺ increased from 4.27×10^{-16} to 1.18×10^{-15} cm² s⁻¹. After 100 cycles, while R_{ct} values of both samples increase because the structural integrity would be compromised inevitably,⁴⁰ the R_{ct} value of the LLO@LBO electrode only increases to 131.6 Ω compared to 209.44 Ω for the undoped LLO case. This indicates that the LLO@LBO electrode has a more stable structure benefiting from boron doping, and leads to a relatively low R_{ct} value and enhanced electrochemical performance.⁴⁰ Furthermore, after 100 cycles the Nyquist plots of LLO and LLO@LBO show distinct differences. Extra semicircles at high-frequency parts are observed in the Nyquist plots of LLO (Fig. 3d). But the Nyquist plot of LLO@LBO after 100 cycles presents a similar shape to that before cycling (Fig. 3d). The appearance of the second semicircle (corresponding to $R_{si} = 116.97 \Omega$) of the LLO electrode after 100 cycles suggests an unstable surface

structure. It could be related to the oxygen loss during cycling. In the case of the LLO@LBO electrode, the initial pattern of EIS remains unchanged, indicating a much improved structural stability.⁴⁰

The thermal stability of cathode materials is closely related to the battery safety. Therefore, differential scanning calorimetry (DSC) measurements of LLO and LLO@LBO electrodes were carried out at the fully charged state of 4.6 V without further treatment. The obtained DSC profiles are presented in Fig. S10.† For LLO, the exothermic reaction initiated at around 218 °C, but it was delayed to 231 °C with an obvious decrease in heat release (628.08 and 192.02 J g⁻¹ for LLO and LLO@LBO, respectively) after boron doping. It is expected that the existence of B–O bonds with high covalency would stabilize the oxygen framework and enhance the battery safety.²⁵

Mechanism for the improved electrochemical performance of LLO@LBO

To investigate the effect of boron doping in detail, we conducted the first-principles calculation to study the process of TM migration during the initial charging process. Fig. 4a shows the migration path of TMs, from octahedral sites at the TM layer to tetrahedral sites at the lithium layer.⁸ Considering the high Mn content in LLO, we focus on the migration process of Mn to understand TM migration. We chose six sites from the migration path and calculated the energy of Mn ions at each site

(Fig. 4b). The energy of Mn ions in LLOs went down at the beginning of the migration process, which means that Li ion extraction accelerates Mn migration. In contrast, the energy decrease of Mn ions at the beginning of migration has not been observed in LLO@LBO. This indicates that the introduction of boron could enhance the structural stability of LLO@LBO, consistent with the results of EIS (Fig. 3d and e) and DSC (Fig. S10, ESI†). Importantly, the energy barrier of Mn ion migration in LLO@LBO is six times that for the LLO case, indicating that the introduction of boron impedes the Mn migration process significantly, though the two cases have similar Mn ion migration path.

Ex situ XRD at different states of charge was conducted to study the variation of crystal structure. The XRD patterns (Fig. 1) of LLO show three major peaks, (003), (101) and (104),³⁵ and their positions are labelled with different colours in Fig. 4d. Among them, the (003) lattice plane is closely related to the electrochemical performance because the transportation of Li ions is along this plane.¹⁰ Therefore, we've focused on the (003) lattice plane spacing variation at different states of charge to understand the effect of boron doping (Fig. 4c). As the cell is being charged, the (003) lattice plane spacing increases gradually. It is attributed to the increasing electrostatic repulsion between oxygen slabs due to the extraction of Li⁺ from the Li layers.⁴¹ When charged beyond 4.4 V, the lattice plane spacing of LLO@LBO continually increases while that of LLO shows no further increase. Previous studies have proved that activation of

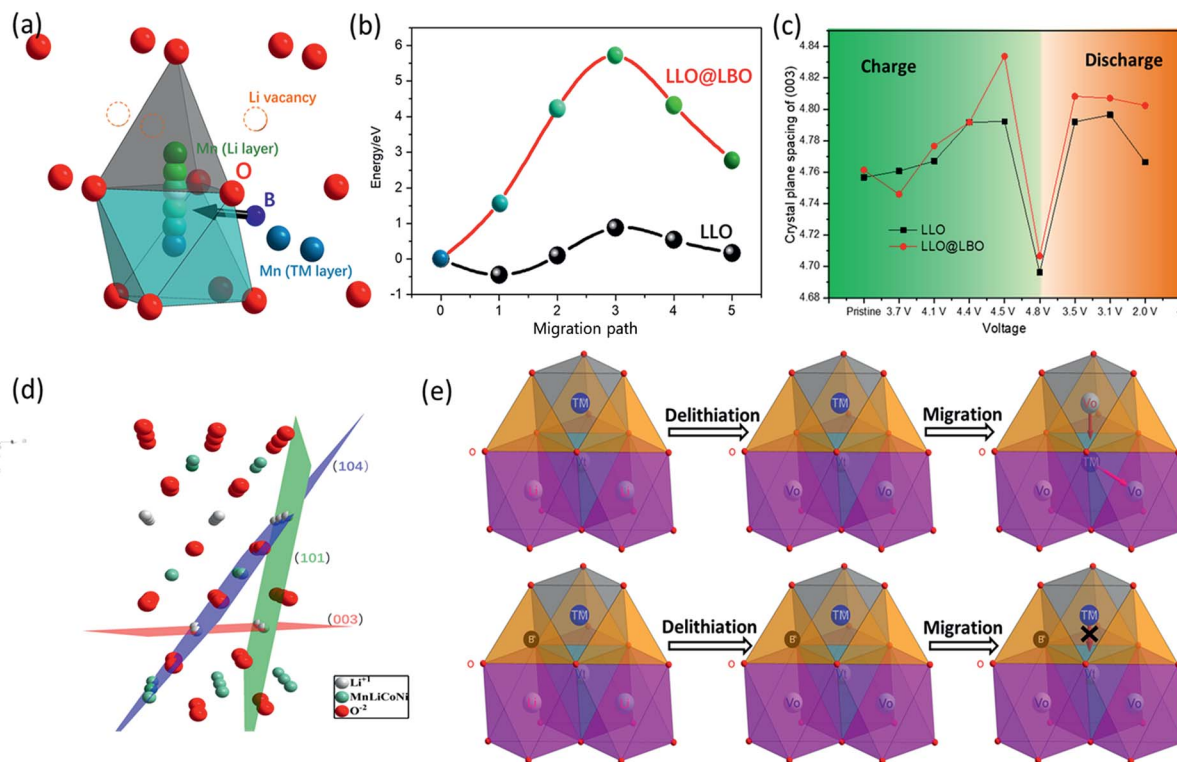


Fig. 4 (a) The migration module of Mn in LLO@LBO. (b) The energy of Mn at different positions in LLO@LBO and LLO. (c) Crystal plane spacing of (003) at different charge/discharge states. (d) Illustration of the atomic configuration and reflection planes of (104), (003) and (101) in the layered structure. (e) Schematic diagrams of the phase evolution routes for LLO and LLO@LBO and it was built on an O3 layered model with unrealistic radii ratios, V_o and V_t stand for octahedral vacancy and tetrahedral vacancy, respectively.

the Li_2MnO_3 phase is accompanied by TM migration, which occurs at the special voltage plateau (around 4.5 V).⁴² Thus, we believe that the migration of TM ions from TM layers to Li layers would reduce the (003) lattice plane spacing due to the electrostatic attraction of the cations and anions. This would neutralize the effect of the extraction of Li^+ from the Li layers and results in unchanged lattice plane spacing. For our B doped material LLO@LBO, the continually increased lattice spacing indicates that the Mn ion migration is mitigated. This agrees with the results of the first-principles calculation shown in Fig. 4b. When charged to 4.8 V, the (003) lattice plane spacing shows a sudden decrease for both LLO and LLO@LBO. This is consistent with the previous work,⁴³ which results from the deconstruction of the framework of the lattice structure. At the following discharging process, the (003) lattice plane spacing rises back and then decreases slowly due to the Li ion reinsertion. Note that the (003) lattice plane spacing at the end of the discharging process is larger than the pristine value for both LLO and LLO@LBO. This could be caused by the increasing electrostatic repulsion between oxygen slabs due to the irreversible lithium loss from the lithium layer. Nevertheless, the (003) lattice plane spacing of LLO@LBO is still larger than that of LLOs during the discharging process due to the difference of TM migration in these two cases.

Based on the results of the first-principles calculations (Fig. 4b) and *ex situ* XRD (Fig. 4c), a schematic diagram is shown in Fig. 4e to understand the effect of boron doping on TM ion migration. Voltage fading causes continuous energy density decay during cycling and limits the performance of LLOs seriously.⁴⁴ It is usually ascribed to the irreversible phase transformation from the layered structure to the spinel structure induced by the migration of TMs.¹⁰ During the charging process, the Li^+ ions are extracted from the LLO cathode gradually, and Li vacancy increment accelerates the TM migration from the octahedral sites of the TM layer to the tetrahedral sites of the lithium layer and then to the octahedral sites of the lithium layer. In the following discharging process, lithium ions reinsert into the lattice and occupy the tetrahedral sites at the Li layer due to the effect of migrated Mn ions,⁴⁵ resulting in the formation of the spinel structure and voltage fading.⁴² For LLO@LBO, boron atoms are doped into the tetrahedral sites of the TM layer and hinder the migration of TMs greatly due to the strong repulsion between B^{3+} and migrated TM ions. Thus, the voltage and capacity decay are mitigated greatly.

Full cell performance study

While the LLO@LBO material exhibits a significantly improved performance in the half-cell device, it is important to have more reliable evaluation using the full cell device. Obviously, for cycling performance evaluation of this material, the anode material needs to have a long cycling time. Also, considering the high energy density of LLO@LBO, similar or higher energy density is required for the anode material. With these, the anode material SnO_2 was used as it exhibits both high energy density and long cycling time,⁴⁶ with the combination of reduced graphene oxide (rGO) to compromise the volume

change during the cycling of SnO_2 . The SEM images are shown in Fig. S11a† and the SnO_2 particles are distributed uniformly in the rGO host. Electrochemical performance test shows that SnO_2 @rGO anode materials deliver an initial CE of 81% and a stable specific capacity of around 750 mA h g^{-1} at 0.5 A g^{-1} (Fig. S11b and c, ESI†). Thus, LLO@LBO was coupled with SnO_2 @rGO as the anode material in a lithium ion full cell to investigate the electrochemical performance of LLO@LBO. Furthermore, Sn element can be used as an internal standard substance to reduce the experimental error for ICP (Inductively Coupled Plasma) analysis of Mn content.

Fig. 5a shows the initial charge/discharge profiles of the full cell LLO// SnO_2 @rGO and LLO@LBO// SnO_2 @rGO. The reversible specific capacity of LLO@LBO// SnO_2 @rGO is $196.4 \text{ mA h g}^{-1}$ based on the mass of cathode materials, much larger than that of $173.8 \text{ mA h g}^{-1}$ for the full cell LLO// SnO_2 @rGO and indicating the enhanced specific capacity due to the boron doping. As a result, the initial coulombic efficiency increased from 64.2% to 73.7%. Fig. 5b shows the cycle performance of full cells LLO// SnO_2 @rGO and LLO@LBO// SnO_2 @rGO. The discharge energy density of LLO@LBO// SnO_2 @rGO is as high as $472.1 \text{ W h kg}^{-1}$ at 0.05C based on the total mass of anode and cathode materials. Moreover, it still retains an energy density of $323.9 \text{ W h kg}^{-1}$ after 150 cycles at 0.5C with energy retention of

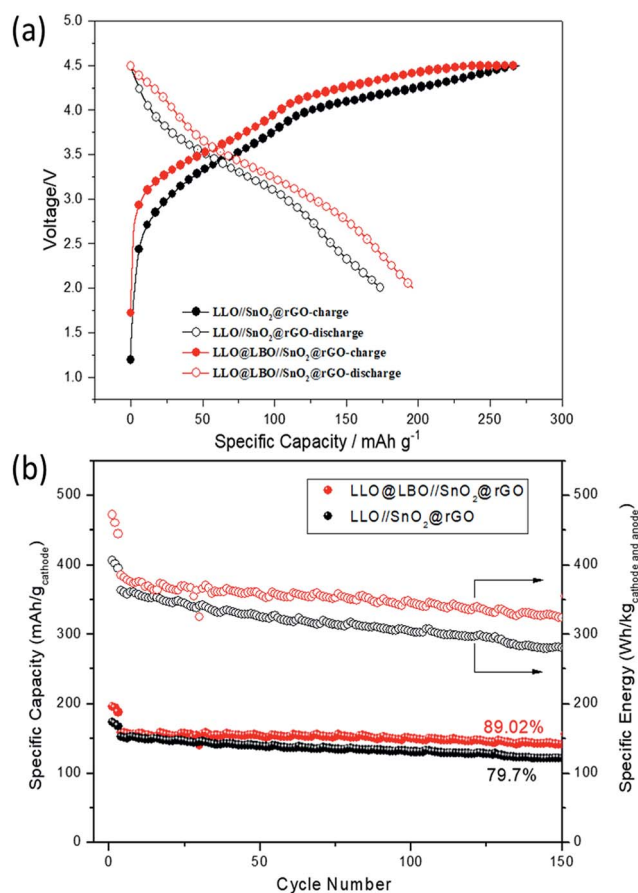


Fig. 5 (a) Charge/discharge profile at the initial cycle of full cells LLO// SnO_2 @rGO and LLO@LBO// SnO_2 @rGO. (b) The cycle performance and energy retention of LLO@LBO// SnO_2 @rGO and LLO// SnO_2 @rGO.

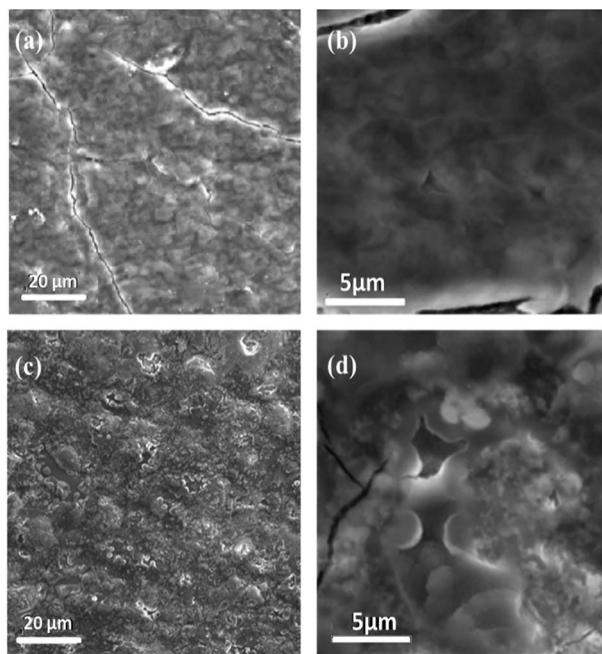


Fig. 6 The morphology of anode electrodes after 20 cycles. (a) LLO@LBO//SnO₂@rGO and (c) LLO//SnO₂@rGO, and their enlarged images (b) and (d), respectively.

84.1%. In contrast, the undoped LLO//SnO₂@rGO only displays an energy density of 406.3 W h kg⁻¹ at 0.05C and 280.3 W h kg⁻¹ after 150 cycles at 0.5C with energy retention of 77.2%. To explore the effect of boron doping on anode electrodes, the morphology of the cycled anode electrodes was characterized by SEM (scanning electron microscopy) (Fig. 6). After 20 cycles, the surface of the anode electrode in LLO@LBO//SnO₂@rGO is still smooth (Fig. 6a and b), indicating a stable SEI structure. In contrast, the surface of that in LLO//SnO₂@rGO became rough and filled with embossments and hollows (Fig. 6c and d). Previous reports have indicated that the surface roughness and erosion during the cycling is due to the reduction of Mn²⁺, which causes Mn metal deposition on the surface of the anode electrode.^{47–49} Furthermore, since Mn metal has higher reactivity than graphite materials, the deposited Mn could catalyse and cause solvent decomposition, further limiting the cycling time.^{50–52} Therefore, we believe that the large difference in the morphology of LLO and LLO@LBO electrodes results from the different levels of Mn²⁺ dissolution of the cathode electrode. Based on this, the ICP experiment of the cycled anode electrodes was carried out to detect the Mn content. The ICP (Table 1) demonstrates that the Mn/Sn ratio (Sn as the internal standard substance) of the anode electrode decreases from 0.195 to

Table 1 ICP results with regard to the content of Mn and Sn in the cycled anode electrode of full cells LLO//SnO₂@rGO and LLO@LBO//SnO₂@rGO

	Mn (mmol L ⁻¹)	Sn (mmol L ⁻¹)	Mn/Sn
LLO//SnO ₂ @rGO	0.024	0.123	0.195
LLO@LBO//SnO ₂ @rGO	0.006	0.086	0.070

0.070 after boron doping, indicating the enhanced structural stability of the doped LLO@LBO.

Conclusions

We have demonstrated that boron doped LLOs show improved discharge capacity and cycle performance, suppressed migration and dissolution of Mn ions and enhanced structural stability. Firstly, the strong B–O bonds can stabilize the oxygen framework of LLOs and improve the structural stability, which can reduce oxygen loss and suppress the side reactions, resulting in improved initial coulombic efficiency. Secondly, the boron atoms occupy the tetrahedral sites at the TM layer, enlarging the migration energy barrier of TM ions during the charging process effectively. This should play a key role in inhibiting voltage fading. Both of them are critical factors of the cycle performance improvement of LLO@LBO in the half cell. As a result, the doped material LLO@LBO delivers a reversible capacity of 293.9 mA h g⁻¹ with a capacity retention of 89.5% at 0.5C after 100 cycles in the half cell. Moreover, the full cell LLO@LBO//SnO₂@rGO also shows improved reversible energy density and energy retention compared to LLO//SnO₂@rGO. Besides the superior cycle performance of the cathode and anode materials, the results of ICP and SEM demonstrated that the Mn ion dissolution is suppressed after boron doping. The full cell LLO@LBO//SnO₂@rGO shows a high initial energy density (472.1 W h kg⁻¹) with excellent energy retention (84.1% retention after 150 cycles at 0.5C). The studies of the effect of boron doping on LLOs in half and full cells are crucial to further explore the Li-ion batteries with higher energy density and longer cycle life which can meet the ever-growing safety requirements.

Experimental section

Synthesis of Li_{1.2}Ni_{0.13}Co_{0.13}Mn_{0.54}O₂ (LLO) and boron doped Li_{1.2}Ni_{0.13}Co_{0.13}Mn_{0.54}O₂ (LLO@LBO)

Li-rich layered oxide, Li_{1.2}Ni_{0.13}Co_{0.13}Mn_{0.54}O₂, was synthesized by oxalic acid co-precipitation, hydrothermal and calcination processes modified based on ref. 53. Firstly, stoichiometric amounts of CH₃COOLi·2H₂O (10% excess), Ni(CH₃COO)₂·4H₂O, Co(CH₃COO)₂·4H₂O and Mn(CH₃COO)₂·4H₂O were dissolved in an ethanol solution together, and the resulting solution was continuously stirred at room temperature for 0.5 h. Oxalic acid was added drop by drop into the mixed ethanol solution as a precipitating agent. The obtained mixture was then transferred into a sealed PTFE (polytetrafluoroethylene) container followed by heating at 180 °C for 12 h. After the hydrothermal reaction, ethanol solvent was removed by vacuum filtration and dried at 120 °C for 3 h. The solid mixture was then pressed into a plate and preheated in air at 450 °C for 5 h and then calcined in air at 850 °C for 15 h. The final product was obtained after uniform grinding. Li_{1.2}Ni_{0.13}Co_{0.13}Mn_{0.54}O₂ was mixed with LiBO₂ by ball milling (500 rpm and 1 h). Afterwards, the solid mixture was pressed into a plate at a pressure of 10 MPa. The plates were then calcined in flowing argon at 700 °C for 2 h. The final product was obtained after uniform grinding.

Characterization

Powder X-ray diffraction (XRD) analysis was performed on a Rigaku D/Max-2500 diffractometer with Cu $K\alpha$ radiation. As for *ex situ* XRD characterization, the samples were prepared by charging (discharging) the cells at constant voltage and then they were disassembled in an argon-filled glove box. The cathode electrode was sealed in polyimide film to avoid reaction with air. DSC measurement (Netzsch-STA 449C) was conducted from room temperature to 300 °C at a heating rate of 10 °C min^{-1} . Samples were prepared by charging the cells at 4.6 V and maintained at a constant voltage for 10 h, and then disassembled in an argon-filled glove box. The cathode material was sealed in an aluminium DSC pan with an additional 1 μL new electrolyte before taking out from the glove box for the measurement. The morphological characteristics were evaluated using scanning electron microscopy (SEM, PhenomPro) and transmission electron microscopy (TEM, JEM-2800). The content of Mn and Sn was detected by inductively coupled plasma-optical emission spectroscopy (ICP-OES, Perkin Elmer, Optima 5300DV) after microwave digestion of the cycled anode electrode. X-ray photoelectron spectroscopy (XPS) was carried out using Escalab 250Xi (Thermo Scientific).

The calculations have been performed using the *ab initio* total energy and molecular dynamics program VASP (Vienna *ab initio* simulation program). Total energy calculations based on density functional theory (DFT) were performed with the exchange and correlation functional form. The interaction of core electrons with the nuclei is described by the projector augmented wave (PAW) method.⁵⁴ A plane wave cutoff energy of 300 eV was used for all calculations. The integration in the Brillouin zone is done on an appropriate k -point set determined by the Monkhorst–Pack scheme. Geometry relaxation of atomic positions with the conjugate gradient algorithm was used to obtain the local minima of the systems. The stopping criteria used were energy differences less than 0.1 meV and forces less than 0.01 eV \AA^{-1} . We used the Nudged Elastic Band method (NEB) implemented in VASP to investigate whether the addition of B in $\text{Li}_{1.2}\text{Ni}_{0.13}\text{Co}_{0.13}\text{Mn}_{0.54}\text{O}_2$ inhibits the migration of lithium ions. Large supercells are required to attain the dilution limit, but since NEB calculations are expensive, the size of the supercell is limited by the computational resources. In the present work, we used Li_3MnO_6 supercells ($2 \times 2 \times 1$) with a $2 \times 2 \times 1$ k -mesh. Constant volume calculations were performed for four intermediate images initialized by linear interpolation between the two fully relaxed end points.

Cell fabrication and electrochemical characterization

Electrochemical measurements were carried out using coin-type cells. To prepare working electrodes, LLO@LBO composite, Super P carbon black, and poly(vinylidene fluoride) (PVDF, in *N*-methyl-2-pyrrolidone) with a mass ratio of 80 : 10 : 10 were mixed to produce a homogeneous slurry and coated onto aluminium foil. After heating at 60 °C for 3 h and 150 °C for 1 h under vacuum, the electrode sheet was pressed and punched into ~ 12 mm diameter electrodes with a mass loading of ~ 2.5 mg. The CR2430 coin-type cells were assembled in an

argon-filled glove box with lithium metal foil as the counter/reference electrode. CR2430 coin-type full cells with LLO@LBO (LLO) as the cathode material and SnO_2 @rGO as the anode material were also assembled in the high-purity argon-filled glove box. The tested anodes were prepared using similar methods to that of the LLO@LBO electrodes. The resultant anode slurry was dispersed and spread onto the copper foil. Before assembling the full cell, the anode electrodes are treated by a pre-lithiated process with 20 cycles to form a stable SEI and stopped with a delithiated state. The ratio of $C_{\text{anode}}/C_{\text{cathode}}$ is about 1.1 to make full use of the capacity of the cathode electrode. The electrolyte (<http://www.dodochem.com>) was 1 M LiPF_6 in ethylene carbonate (EC) : dimethyl carbonate (DMC) : diethyl carbonate (DEC) (1 : 1 : 1 vol%). Celgard 2325 was used as the separator. The charge/discharge measurements were performed using a battery test system (LAND CT2001A model, Wuhan LAND Electronics. Ltd) over a voltage window from 2.0 V to 4.6 V at room temperature. For the full cell test, the voltage window of 2.0–4.5 V is adopted for activation and the following cycle process. Several low rate (0.05C) cycles at the beginning are always necessary to activate the Li_2MnO_3 phase. Electrochemical impedance spectral (EIS) measurements were recorded using an Autolab system (Metrohm) and carried out at an AC amplitude of 10 mV in the range of 100 kHz to 10 mHz.

Conflicts of interest

There are no conflicts to declare.

Acknowledgements

The authors gratefully acknowledge the financial support from the Ministry of Science and Technology of China (MOST, 2016YFA0200200), the National Natural Science Foundation of China (NSFC, 21421001, 51633002 and 51472124), Tianjin City (16ZXCLGX00100) and 111 Project (B12015).

Notes and references

- 1 B. Qiu, M. H. Zhang, L. J. Wu, J. Wang, Y. G. Xia, D. N. Qian, H. D. Liu, S. Hy, Y. Chen, K. An, Y. M. Zhu, Z. P. Liu and Y. S. Meng, *Nat. Commun.*, 2016, **7**, 12108.
- 2 R. Yu, X. Zhang, T. Liu, L. Yang, L. Liu, Y. Wang, X. Wang, H. Shu and X. Yang, *ACS Appl. Mater. Interfaces*, 2017, **9**, 41210–41223.
- 3 R. A. House, L. Jin, U. Maitra, K. Tsuruta, J. W. Somerville, D. P. Förstermann, F. Massel, L. Duda, M. R. Roberts and P. G. Bruce, *Energy Environ. Sci.*, 2018, **11**, 926.
- 4 R. Yu, X. Wang, D. Wang, L. Ge, H. Shu and X. Yang, *J. Mater. Chem. A*, 2015, **3**, 3120–3129.
- 5 G. Assat, D. Foix, C. Delacourt, A. Iadecola, R. Dedryvère and J.-M. Tarascon, *Nat. Commun.*, 2017, **8**, 2219.
- 6 S. Shi, T. Wang, M. Cao, J. Wang, M. Zhao and G. Yang, *ACS Appl. Mater. Interfaces*, 2016, **8**, 11476–11487.
- 7 J. L. Shi, D. D. Xiao, M. Ge, X. Yu, Y. Chu, X. Huang, X. D. Zhang, Y. X. Yin, X. Q. Yang, Y. G. Guo, L. Gu and L. J. Wan, *Adv. Mater.*, 2018, **30**, 1705575.

- 8 J. M. Zheng, S. J. Myeong, W. R. Cho, P. F. Yan, J. Xiao, C. M. Wang, J. Cho and J. G. Zhang, *Adv. Energy Mater.*, 2017, **7**, 1601284.
- 9 S. Hy, H. D. Liu, M. H. Zhang, D. N. Qian, B. J. Hwang and Y. S. Meng, *Energy Environ. Sci.*, 2016, **9**, 1931–1954.
- 10 D. Mohanty, J. Li, D. P. Abraham, A. Huq, E. A. Payzant, D. L. Wood and C. Daniel, *Chem. Mater.*, 2014, **26**, 6272–6280.
- 11 R.-P. Qing, J.-L. Shi, D.-D. Xiao, X.-D. Zhang, Y.-X. Yin, Y.-B. Zhai, L. Gu and Y.-G. Guo, *Adv. Energy Mater.*, 2016, **6**, 1501914.
- 12 W. K. Pang, H.-F. Lin, V. K. Peterson, C.-Z. Lu, C.-E. Liu, S.-C. Liao and J.-M. Chen, *Chem. Mater.*, 2017, **29**, 10299.
- 13 X. Ding, B. Zou, Y. Li, X. He, J. Liao, Z. Tang, Y. Shao and C. Chen, *Sci. China Mater.*, 2017, **60**, 839–848.
- 14 R. Z. Yu, X. H. Zhang, T. Liu, X. Xu, Y. Huang, G. Wang, X. Y. Wang, H. B. Shu and X. K. Yang, *ACS Sustainable Chem. Eng.*, 2017, **5**, 8970–8981.
- 15 Q. Li, G. S. Li, C. C. Fu, D. Luo, J. M. Fan and L. P. Li, *ACS Appl. Mater. Interfaces*, 2014, **6**, 10330–10341.
- 16 Y. Kou, E. Han, L. Zhu, L. Liu and Z. a. Zhang, *Solid State Ionics*, 2016, **296**, 154–157.
- 17 D. H. Seo, J. Lee, A. Urban, R. Malik, S. Kang and G. Ceder, *Nat. Chem.*, 2016, **8**, 692–697.
- 18 J. Lee, D. A. Kitchaev, D.-H. Kwon, C.-W. Lee, J. K. Papp, Y.-S. Liu, Z. Lun, R. J. Clement, T. Shi, B. D. McCloskey, J. Guo, M. Balasubramanian and G. Ceder, *Nature*, 2018, **556**, 185–190.
- 19 P. Y. Hou, G. R. Li and X. P. Gao, *J. Mater. Chem. A*, 2016, **4**, 7689–7699.
- 20 P. K. Nayak, J. Grinblat, M. Levi, E. Levi, S. Kim, J. W. Choi and D. Aurbach, *Adv. Energy Mater.*, 2016, **6**, 1502398.
- 21 J. Zheng, X. Wu and Y. Yang, *Electrochim. Acta*, 2013, **105**, 200–208.
- 22 L. Li, B. H. Song, Y. L. Chang, H. Xia, J. R. Yang, K. S. Lee and L. Lu, *J. Power Sources*, 2015, **283**, 162–170.
- 23 J. H. Song, A. Kapyloyou, H. S. Choi, B. Y. Yu, E. Matulevich and S. H. Kang, *J. Power Sources*, 2016, **313**, 65–72.
- 24 H.-Z. Zhang, F. Li, G.-L. Pan, G.-R. Li and X.-P. Gao, *J. Electrochem. Soc.*, 2015, **162**, A1899–A1904.
- 25 B. Li, H. Yan, J. Ma, P. Yu, D. Xia, W. Huang, W. Chu and Z. Wu, *Adv. Funct. Mater.*, 2015, **24**, 5112–5118.
- 26 J. B. Goodenough and K. S. Park, *J. Am. Chem. Soc.*, 2013, **135**, 1167–1176.
- 27 X. Li, K. Zhang, D. Mitlin, Z. Yang, M. Wang, Y. Tang, F. Jiang, Y. Du and J. Zheng, *Chem. Mater.*, 2018, **30**, 2566–2573.
- 28 L. Pan, Y. Xia, B. Qiu, H. Zhao, H. Guo, K. Jia, Q. Gu and Z. Liu, *J. Power Sources*, 2016, **327**, 273–280.
- 29 J. Liu, S. Wang, Z. Ding, R. Zhou, Q. Xia, J. Zhang, L. Chen, W. Wei and P. Wang, *ACS Appl. Mater. Interfaces*, 2016, **8**, 18008–18017.
- 30 R. Alcántara, P. Lavela, J. L. Tirado, R. Stoyanova and E. Zhecheva, *J. Solid State Chem.*, 1997, **134**, 265.
- 31 D. Uzun, *Solid State Ionics*, 2015, **281**, 73–81.
- 32 Y.-S. Hong, Y. J. Park, K. S. Ryu, S. H. Chang and M. G. Kim, *J. Mater. Chem. A*, 2004, **14**, 1424–1429.
- 33 X. Yu, Y. Lyu, L. Gu, H. Wu, S.-M. Bak, Y. Zhou, K. Amine, S. N. Ehrlich, H. Li, K.-W. Nam and X.-Q. Yang, *Adv. Energy Mater.*, 2014, **4**, 1300950.
- 34 J. Zhao, W. Zhang, A. Huq, S. T. Misture, B. Zhang, S. Guo, L. Wu, Y. Zhu, Z. Chen, K. Amine, F. Pan, J. Bai and F. Wang, *Adv. Energy Mater.*, 2017, **7**, 1201266.
- 35 D. Ye, G. Zeng, K. Nogita, K. Ozawa, M. Hankel, D. J. Searles and L. Wang, *Adv. Funct. Mater.*, 2015, **25**, 7488–7496.
- 36 T. Chen, X. Li, H. Wang, X. Yan, L. Wang, B. Deng, W. Ge and M. Qu, *J. Power Sources*, 2018, **374**, 1–11.
- 37 W. E. Gent, K. Lim, Y. Liang, Q. Li, T. Barnes, S.-J. Ahn, K. H. Stone, M. McIntire, J. Hong, J. H. Song, Y. Li, A. Mehta, S. Ermon, T. Tyliszczak, D. Kilcoyne, D. Vine, J.-H. Park, S.-K. Doo, M. F. Toney, W. Yang, D. Prendergast and W. C. Chueh, *Nat. Commun.*, 2017, **8**, 2091.
- 38 Q.-Q. Qiao, G.-R. Li, Y.-L. Wang and X.-P. Gao, *J. Mater. Chem. A*, 2016, **4**, 4440–4447.
- 39 N. Koga and T. Utsuoka, *Thermochim. Acta*, 2006, **443**, 197–205.
- 40 Q.-Q. Qiao, G.-R. Li, Y.-L. Wang and X.-P. Gao, *J. Mater. Chem. A*, 2016, **4**, 4440–4447.
- 41 D. Mohanty, S. Kalnaus, R. A. Meisner, K. J. Rhodes, J. Li, E. A. Payzant, D. L. Wood and C. Daniel, *J. Power Sources*, 2013, **229**, 239–248.
- 42 P. Oh, M. Ko, S. Myeong, Y. Kim and J. Cho, *Adv. Energy Mater.*, 2014, **4**, 1400631.
- 43 S. Shen, Y. Hong, F. Zhu, Z. Cao, Y. Li, F. Ke, J. Fan, L. Zhou, L. Wu, P. Dai, M. Cai, L. Huang, Z. Zhou, J. Li, Q. Wu and S. Sun, *ACS Appl. Mater. Interfaces*, 2018, **10**, 12666–12677.
- 44 J.-L. Shi, J.-N. Zhang, M. He, X.-D. Zhang, Y.-X. Yin, H. Li, Y.-G. Guo, L. Gu and L.-J. Wan, *ACS Appl. Mater. Interfaces*, 2016, **8**, 20138–20146.
- 45 G. Assat and J.-M. Tarascon, *Nat. Energy*, 2018, **3**, 373.
- 46 M. Zhang, Z. Sun, T. Zhang, D. Sui, Y. Ma and Y. Chen, *Carbon*, 2016, **102**, 32–38.
- 47 I. H. Cho, S. S. Kim, S. C. Shin and N. S. Choi, *Electrochim. Solid-State Lett.*, 2010, **13**, A168–A172.
- 48 S. Komaba, N. Kumagai and Y. Kataoka, *Electrochim. Acta*, 2002, **47**, 1229–1239.
- 49 B. Song, Z. Liu, M. O. Lai and L. Lu, *Phys. Chem. Chem. Phys.*, 2012, **14**, 12875–12883.
- 50 H. Shin, J. Park, A. M. Sastry and W. Lu, *J. Power Sources*, 2015, **284**, 416–427.
- 51 C. Zhan, T. Wu, J. Lu and K. Amine, *Energy Environ. Sci.*, 2018, **11**, 243–257.
- 52 L. Li, X. Zhang, R. Chen, T. Zhao, J. Lu, F. Wu and K. Amine, *J. Power Sources*, 2014, **249**, 28–34.
- 53 L. Li, X. Zhang, R. Chen, T. Zhao, J. Lu, F. Wu and K. Amine, *J. Power Sources*, 2014, **249**, 28–34.
- 54 P. E. Blöchl, *Phys. Rev. B: Condens. Matter Mater. Phys.*, 1994, **50**, 17953–17979.